Appl. Phys. B 77, 391–397 (2003)
DOI: 10.1007/s00340-003-1262-z

Applied Physics B
Lasers and Optics

A. ASSION[1]
M. WOLLENHAUPT[1]
L. HAAG[1]
F. MAYOROV[1]
C. SARPE-TUDORAN[1]
M. WINTER[1]
U. KUTSCHERA[2]
T. BAUMERT[1,✉]

Femtosecond laser-induced-breakdown spectrometry for Ca^{2+} analysis of biological samples with high spatial resolution

[1] Fachbereich für Naturwissenschaften und Center of Interdisciplinary Nanostructure Science and Technology (CINSaT), Institut für Physik[1], Institut für Biologie[2], Universität Kassel, 34109 Kassel, Germany

Received: 1 July 2003
Published online: 10 September 2003 •

ABSTRACT We describe an analytical method for element-specific *in situ* investigations of biological samples with high spatial resolution, using laser-induced-breakdown spectroscopy (LIBS). The prerequisites for spatially highly resolved LIBS are an appropriate analytical performance in combination with precise micro-ablation conditions, both laterally and axially. In order to identify the best suitable laser source, the analytical performance and the ablation process were studied for ns-LIBS and fs-LIBS. The analytical performance was studied on an aqueous solution of $CaCl_2$, where water served as a first substitute for biological material. The ablation process was investigated in the outer epidermal wall of a sunflower seedling stem. Besides direct measurements, the physiology of the sunflower seedling can be used in order to estimate the ablation depth. Our results show that analytical measurements with high spatial resolution can be performed on biological samples using fs-LIBS. This was demonstrated by in situ measurements of wall-associated calcium ion (Ca^{2+}) distributions within the peripheral cell wall of the sunflower seedling (*Helianthus annuus* L.) stem. In this biological sample an axial resolution of about 100 nm was achieved.

PACS 52.50.Jm; 42.62.Be; 78.47.+p; 87.16.-b

1 Introduction

The objective of this work is the development of a minimal invasive analytical method for spectrochemical *in situ* investigations of biological samples, with an axial resolution in the range of 100 nm, employing laser-induced-breakdown spectroscopy (LIBS).

Several decades ago, LIBS was established as a spectrochemical analysis method, where a laser-induced plasma is used as a spectrochemical source. The fundamental advantages of this approach can be summarized as follows: no sample preparations are necessary, remote sensing measurements are possible and samples of any state of aggregation can be analyzed. The method is sensitive to the detection of different chemical elements. Moreover, multi-element analysis can be performed. Sensitivity limits in the ppm range can be achieved and spatial information can be obtained [1]. Mainly ns lasers have been used for LIBS and primarily analytical questions have been addressed. Only a few LIBS studies have investigated the spatial resolution from a basic point of view [2–5].

If spatial resolution becomes important, laser ablation processes have to be taken into account in addition. For transparent media and laser sources operating in the visible and infrared, ablation is initiated by the generation of a critical density of free electrons. Employing ultra-short laser pulses, multiphoton ionization is the dominating free electron formation path [6]. The non-linear dependence of multiphoton ionization on the laser intensity results in a sharply defined threshold for the optical breakdown. Additionally, during the interaction with the ultra-short laser pulse the energy absorbed by the electrons is not transferred to the lattice. For ns-laser pulses, the electron plasma is generated by collisional (avalanche) ionization [7]. Statistical fluctuations of the number of starting electrons for the avalanche ionization lead to strong fluctuations of the damage threshold. Therefore, in comparison to ns lasers, the optical breakdown threshold for fs lasers is a well-defined quantity. The breakdown threshold energy decreases with the fs-laser-pulse duration. Precise ablation, i.e. low ablation rates and minimal collateral damage, can be achieved, not only for technical [8–17] but also for biological samples [18–21].

Based on these considerations it is natural to assume that fs lasers are the ideal tool for minimal invasive LIBS with high spatial resolution. However, extensive experimental experience on LIBS, demonstrating the high sensitivity of this method, exists mainly for ns-laser systems. With fs-laser systems only a few experiments have been carried out, in which the plasma dynamics of fs-laser-generated plasmas of metallic samples was investigated [22–24].

From the discussion above, it is not obvious what kinds of laser sources enable LIBS with high sensitivity and high spatial resolution simultaneously, where sample volumes in the order of femtoliters and below have to be analyzed. Therefore, we investigated which laser source (fs laser or ns laser) is more suitable for LIBS with high spatial resolution.

This paper is composed of four parts. In Sect. 2, the experimental setup and the biological sample are described. Section 3 deals with basic considerations concerning the spatial resolution of LIBS. In Sect. 4, the analytical performances of ns-LIBS and fs-LIBS are discussed. In Sect. 5, a biological

✉ Fax: +49-561/804-4453, E-mail: baumert@physik.uni-kassel.de

application for fs-LIBS is presented, demonstrating spatially highly resolved trace-element analysis with an axial resolution of about 100 nm.

2 Experimental

2.1 *Experimental setup*

The schematic setup of the LIBS system is shown in Fig. 1. As laser source either a commercial Nd : YAG ns laser (Quanta-Ray Indi, Spectra-Physics, USA) or a Ti : sapphire fs-laser system (Femtopower Pro, FEMTOLASERS, Austria) is employed. The ns laser generates laser pulses with a pulse duration of 6 ns and a maximum pulse energy of 385 mJ at 1064 nm, 140 mJ at 532 nm and 30 mJ at 355 nm. The repetition rate is 20 Hz. For the biological applications, low penetration depths are required. Therefore, the ns-laser experiments are performed at 355 nm. Representative results are shown and discussed in Sect. 4. The fs-laser system generates 30 fs laser pulses at a central wavelength of 790 nm with a maximum pulse energy of 1 mJ and a repetition rate of 1 kHz.

The fs-laser-beam path is integrated in a modified confocal laser scanning microscope (CLSM-DIAPLAN, Leica, Germany). After passing a dichroic beam splitter (DBS) the laser beam is tightly focused onto the sample with a numerical aperture (NA) = 0.4 objective (O) (LD Epiplan, Zeiss, Germany). The relatively low NA minimizes damage risks of the objective and allows a convenient working distance of 10 mm. In order to obtain the shortest fs-laser pulse the group delay introduced by the dispersive elements in the beam path was compensated by means of a prism compressor. An interferometric autocorrelation was measured using a two-photon diode placed in the focal plane of the objective. The residual pulse-front distortion due to chromatic and spherical aberration [25] leads to a spatially averaged pulse duration of 40 fs. For the ns laser, a similar setup is used. The NA = 0.4 objective is replaced by a fused-silica lens ($f = 15$ mm), because of the low transmission of the objective. The beam profile of the ns laser and the fs laser in the focal plane was measured with the cutting edge method. For the fs-laser- and ns-laser-beam profiles, beam waists of 2.0 ± 0.1 μm and 30 ± 3 μm, respectively, were found. Due to the astigmatism of the fs-laser beam and the non-Gaussian ns-laser beam the measured beam waists are larger than the expected theoretical beam waists.

The generated plasma luminescence (PL), efficiently collected with the focusing objective or lens (O/L), and reflected from a dichroic beam splitter (DBS), is imaged with an objective (105 mm, UV-Nikkor, Nikon, Japan) on the entrance slit (280 μm) of a spectrograph (MS125, Oriel, USA). The spectral distribution of the plasma luminescence is measured with an intensified charge-coupled-device (ICCD) camera (Flame Star, LaVision, Germany) within a variable time window after the plasma formation. The time window is controlled with a delay generator (DG 535, Stanford Research, USA). For single-shot measurements, the repetition rate of the ns-laser and the fs-laser system is adapted to the maximum repetition rate of the ICCD used in our setup (1 Hz).

The position of the sample is controlled via a conventional light microscope. For precise sample positioning, a computer-controlled piezo-driven *xyz* table (P-527.3CD, Physik Instrumente, Germany) is used. For the ablation experiments an interference microscope (Newview 5000, Zygolot, Germany) is used, to measure the ablation volume.

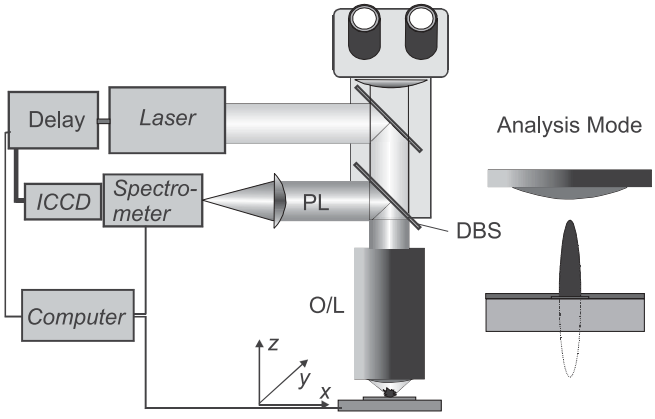

FIGURE 1 *Left:* schematic setup of the laser-induced-breakdown spectrometry (LIBS) system. Either a ns-laser system or a fs-laser system was used for the experiments. The LIBS detection is integrated in a confocal microscope setup. The fs-laser beam is tightly focused with a NA = 0.4 objective (O). For the ns-laser beam a fused-silica lens (L) ($f = 15$ mm) is used. The same objective/lens is used to efficiently collect the plasma luminescence (PL). The PL reflected from a dichroic beam splitter (DBS) is recorded spectrally resolved with an ICCD camera. The sample positioning can be controlled with a conventional light microscope. A precise positioning of the sample is achieved by a piezo-driven *xyz*-translation stage. *Right:* schematic dimensions of above-threshold volume (see Fig. 4) with respect to the epidermal cell wall (see Fig. 3)

2.2 *Biological sample: the sunflower seedling*

For the experimental analysis of the mechanism of cell elongation the rapidly growing, sturdy seedlings of the sunflower (*Helianthus annuus* L.) are a classical model system [26]. About 50 seeds (achenes) of *Helianthus annuus* L. cv. Giganteus were soaked for 1 h in distilled water and thereafter planted in moist vermiculite in closed plastic boxes at 25 °C in a 12 h light/12 h dark cycle as described [34]. The photon flux density at plant level was about 100 μmol m^{-2} s^{-1}. For all experiments described below 6-day-old green sunflower seedlings of average size were used. The general morphology of such a juvenile plant is shown in Fig. 2a. The peripheral cell layer (epidermis) of the hypocotyl (axis between the onset of the root and the cotyledons) was selected as a target for our studies, because this specific tissue represents the growth-limiting structure of the organ [34]. A surface view of the epidermis shows that this tissue is composed of two types of cells: epidermal cells (average dimensions: length ≈ 150 μm, width ≈ 16 μm) and the much shorter guard cells of the stomata (pores for gas exchange with the environment) (Figs. 2b and 3a). The epidermis of the sunflower stem (hypocotyl) is characterized by a thick, sturdy cellulosic structure, the outer epidermal wall. In 6-day-old green sunflower stems, this particular wall has an average thickness of 1.5–2.0 μm [26]. However, as Fig. 3b shows, in the corners between the adjacent epidermal cells, the wall thickness can reach twice that value. Taken together, these ultra-structural

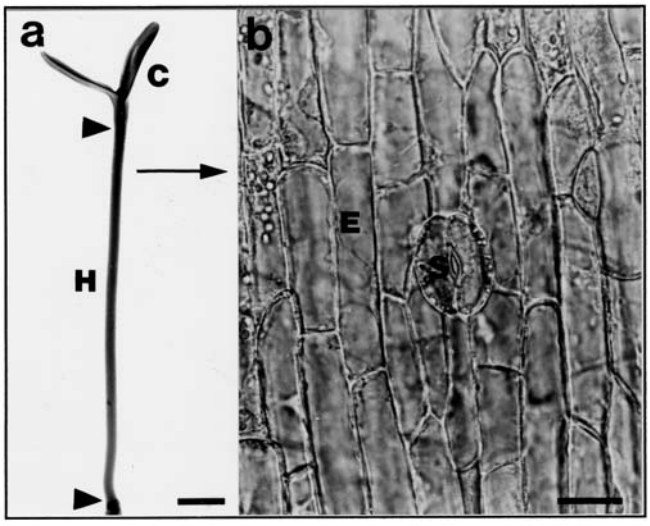

FIGURE 2 Photographs of a 6-day-old green sunflower seedling (a) and the peripheral cell layer in the sub-apical region of the stem (b). The juvenile plant (a) consists of three organs: the root (region below the *lower arrowhead*), the stem (hypocotyl, H) and the cotyledons (C). The onset of these leaf-like structures is indicated by the *upper arrowhead*. The peripheral tissue (b) is composed of epidermal cells (E) and stomata (S). *Bars*: 10 mm (a), 20 μm (b)

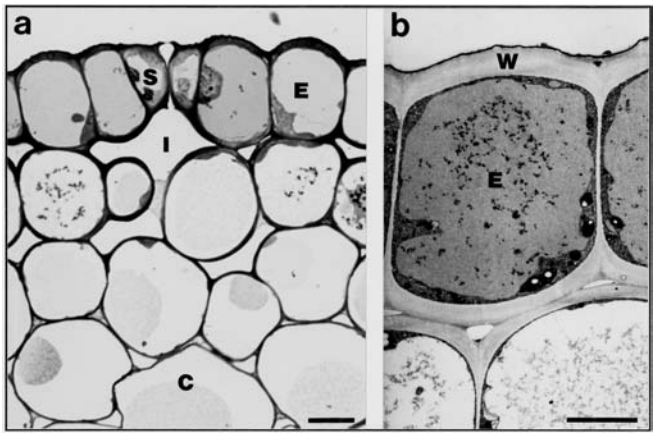

FIGURE 3 Light (**a**) and electron micrograph (**b**) of transverse sections through the sub-apical region of a sunflower hypocotyl (see Fig. 2a). c = cortical cell, E = epidermal cell with vacuole and peripheral cytoplasm, I = intracellular space, S = stoma (guard cell), W = outer epidermal wall. *Bars*: 10 μm (a), 5 μm (b)

data demonstrate that our biological material (outer epidermal wall of 6-day-old sunflower hypocotyls) is heterogeneous.

The three basic requirements for our analysis can be summarized as follows: (i) all experiments have to be performed on intact stems (*in situ*), (ii) the concentration of bound calcium ions (< 100 mmol/l) inside the peripheral cell-wall structure should be resolved and (iii) the axial resolution should be in the range of 100 nm. In particular, the necessary axial resolution is the experimental challenge for any kind of analytical method with high spatial resolution.

3 Basic considerations about spatial resolution

In order to generate a plasma which can be spectroscopically analyzed the laser fluence has to be above the optical breakdown threshold of the sample. Therefore, the spatial resolution can be estimated by the extent of the laser fluence in the focus, which exceeds the optical breakdown threshold (above-threshold zone). The laser fluence in the vicinity of the focus is proportional to the point spread function (PSF) of the objective. If one assumes homogeneous illumination of the aperture of a low-NA objective, the PSF can be calculated as described in [27]. In Fig. 4 the PSF for a NA = 0.4 objective is shown. The ratio $c = \Phi_{\text{threshold}}/\Phi_{\max}$ of the optical breakdown threshold fluence $\Phi_{\text{threshold}}$ and the maximum laser fluence $\Phi_{\max}$ determines the above-threshold zone. For $\lambda = 790$ nm, NA = 0.4 and $c = 0.9$ a threshold radius of $r_{\text{threshold}} = 200$ nm is obtained (see Fig. 4a). For example, the Rayleigh criterion for a standard microscope or a confocal microscope results in a lateral resolution of 1.2 μm and 1.1 μm, respectively [28, 29].

This comparison shows that with the use of LIBS at a fluence close to the threshold limit a higher lateral resolution compared to conventional or confocal microscope techniques can be obtained.

Because of the relation between the lateral and the axial distributions of the PSF – for the above-threshold zone – the same holds true for the axial resolution. The cigar-like contour lines shrink with $\Phi_{\max}$ approaching $\Phi_{\text{threshold}}$ (see Fig. 4b). However, when employing such a mode of operation (imaging mode), the demanded axial resolution of around 100 nm cannot be achieved, since unrealistic c values of around 0.9999 would be necessary. Small-amplitude fluctuations of the laser

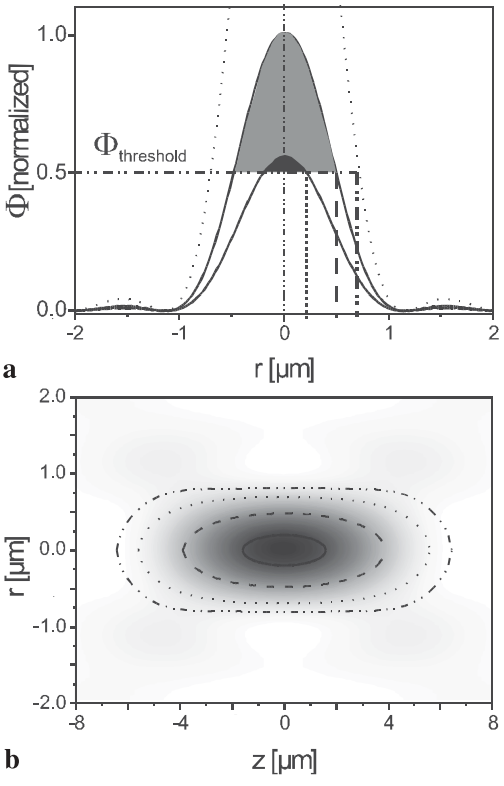

FIGURE 4 **a** Lateral cross section through the point spread function (PSF) in the focal plane for a NA = 0.4 objective. The lateral above-threshold radius is shown for $c = 0.5$ ($c = \Phi_{\text{threshold}}/\Phi_{\max}$) (*blank–blank*) and $c = 0.9$ (*dotted line*). **b** PSF in the z, r plane and contour lines confining the above-threshold zone for different c values ($c = 0.1$ *blank–dot–dot–blank*, $c = 0.2$ *dotted*, $c = 0.5$ *blank–blank*, $c = 0.9$ *blank*)

or minimal changes in the threshold values would preclude reproducible results.

In order to achieve high axial resolution a different approach with lower c values is employed, since the plasma formation is accompanied by ablation. The axial zone where a plasma is formed is determined by the ablation depth. For example, if a structured thin layer has to be analyzed, the ablation depth of each laser shot has to be smaller than the layer thickness. Moreover the spectrochemical analysis has to be performed on a single laser shot basis. For this analysis mode it is not required to change the position of the sample for depth profiling. A schematic sketch of this analysis mode is shown in Fig. 1.

Assuming nearly constant plasma-generation and ablation-rate conditions, a precise spectrochemical measurement within each layer is possible. The axial resolution can be in the order of a few tens of nanometers or less for technical materials [5]. In order to obtain a constant ablation volume for each laser pulse the above-threshold area along the axial direction must not change significantly inside the layer. This focusing condition can be achieved by employing a laser fluence a few times higher than the threshold fluence. As illustrated in Fig. 4b, for $c = 0.2$ the cigar-like contour line shows no dependence on the lateral coordinate in the axial range of $\pm 2\,\mu$m.

In order to simultaneously obtain small ablation depth and plasma conditions suitable for spectrochemical analysis we investigated the role of laser parameters, i.e. pulse duration and fluence.

4 Comparison of fs-laser- and ns-laser-induced breakdown spectroscopy

4.1 *Analytical performance studies*

Ca^{2+} detection in water with ns- and fs-LIBS has been studied explicitly. The setup is displayed in Fig. 1. A water-jet table was used as the sample. It serves as a calibrated Ca^{2+} source and can be considered as a first model system of a biological sample. The nozzle for the water jet was mounted on the piezo-driven *xyz* table. The laser pulses were focused on the water-jet surface. In order to achieve well-resolved Ca^{+} lines, the spectral region around 395 nm was chosen for the measurements. The two strong Ca^{+} lines at 393.4 nm and 396.8 nm can be resolved, corresponding to a Ca^{+} ($3p^6 4s - 3p^6 4p$) transition. At physiologically relevant concentrations (1–100 mmol/l) linear Ca^{2+}-calibration curves are measured with fs- and ns-LIBS. The sensitivity limit for fs-LIBS is determined by the maximum fs-laser-pulse energy (180 μJ, corresponding to a laser fluence in the focal plane of 2870 J/cm^2), which leaves the object intact. With our detection system a sensitivity limit of 0.4 mmol/l can be found. For ns-LIBS a sensitivity limit of 0.1 mmol/l can be reached with a laser energy of 30 mJ (2130 J/cm^2).

The transient plasma luminescence spectra are illustrated in Fig. 5 and reveal the plasma dynamics in the case of ns- or fs-laser excitation. For both experiments the same detection system with identical ICCD camera settings was used and the same Ca^{2+} concentration of 20 mmol/l was taken. The appearance of plasma luminescence in the range of 380 nm to 400 nm was employed to determine the plasma-generation threshold. In the case of the fs laser a threshold of 6.7 ± 0.7 J/cm^2 was measured for the plasma formation. The transient plasma luminescence spectra (Fig. 5a) were measured with a laser fluence of 1.7 times the threshold. The transient is dominated by the Ca^{+}-line emissions. The best signal to background ratio can be found at the onset of the plasma formation.

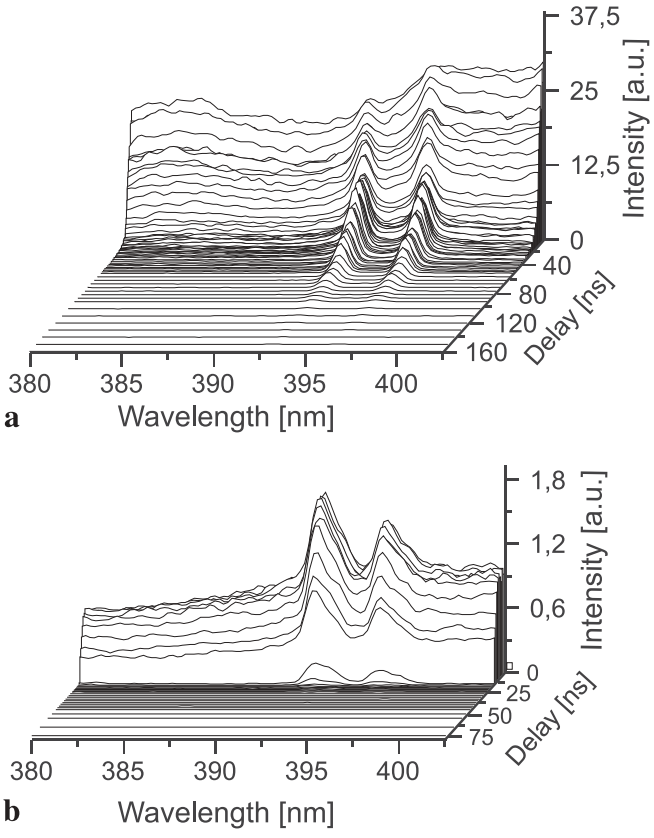

FIGURE 5 Plasma-emission transients from water upon excitation with **a** fs-laser pulses (40 fs, 790 nm, 11 J/cm^2 averaged over 1000 laser shots) and **b** ns-laser pulses (6 ns, 355 nm, 120 J/cm^2, averaged over 20 laser shots). The plasma luminescence was integrated within a time window of 15 ns in time steps of 1 ns, 5 ns and 10 ns. In both experiments the Ca^{2+} concentration was 20 mmol/l

In the case of the ns laser a threshold of 70 ± 15 J/cm^2 was found for the plasma formation. In order to measure the transient luminescence plasma spectra (Fig. 5b) the same above-threshold ratio of 1.7 was chosen. Nevertheless, the continuum emission is much stronger. At the beginning of the plasma formation the continuum emission dominates the spectra. A strong contribution of Ca^{+}-line emission starts to appear after around 10 ns. The best signal to background ratio was found at 28 ns.

For ns-LIBS a generally accepted picture to describe the plasma luminescence emission exists [1]. An intense ns laser with pulse energies in the 100 mJ regime generates an electron–ion plasma, which expands at a velocity much faster than the speed of sound. The electron temperature decreases and after several microseconds the plasma decays through radiative, quenching and electron–ion recombination processes. Because in our experiment the ns-laser-pulse energy was chosen close to the threshold value for plasma generation, the Ca^{+}-line emission starts to appear al-

ready at the beginning of the plasma formation. However, the same mechanism of a delayed strong Ca^+-line emission was observed.

Although identical camera settings (besides the averaging) were used for the fs laser, the Ca^+-line emission dominates the continuum emission from the beginning of the plasma formation, indicating that the plasma temperature was significantly lower. This is supported by the fact that the continuum emission relative to the Ca^+-line emission is strongly reduced in the case of the fs laser. Similar results for technical samples are observed where a faster thermalization of fs-laser-generated plasmas was found [30].

For fs-laser and ns-laser excitation, different plasma-formation models in transparent media exist. Recent theoretical and experimental investigations showed that this model can also be applied to water [31, 32]. For ns lasers, avalanche ionization is the dominant plasma-formation path. Multiphoton ionization is responsible only for the generation of seed electrons for the avalanche ionization. In contrast, for fs-laser excitation the plasma is generated mainly due to multiphoton ionization [32]. As the multiphoton ionization rate increases with the intensity, less pulse energy is necessary for ultrashort laser pulses to generate a plasma. Moreover, Vogel et al. [33] have shown that the conversion of laser light energy into mechanical energy during optical breakdown is dramatically reduced for fs-laser pulses. This indicates why fs-LIBS of water samples close to the plasma-generation threshold can be performed with the same analytical resolution as in the case of ns-LIBS but with a laser fluence an order of magnitude lower.

Due to the lower laser fluence required for fs-LIBS and the reduced plasma temperature a significant decrease of the ablation volume and minimal collateral damage of the sample are observed. This topic will be discussed in Sect. 4.2.

4.2 *Ablation studies*

The ns-laser versus fs-laser ablation experiments on biological samples have been carried out with 6-day-old sunflower seedlings (Fig. 2a). The physiology of the sunflower seedling can be employed directly to estimate the ablation depth. Inside the cells of the stem (hypocotyl) a multidirectional hydrostatic pressure, called turgor pressure, of around 0.55 MPa was measured [34]. As illustrated in Fig. 3a and b, the peripheral wall acts like a giant wall sheath, which encloses the protoplasts of the cells that are surrounded by thin, extensible walls. If laser ablation destroys the peripheral wall, cell sap is pressed out of the protoplast (vacuole), which is visible in the light microscope.

In order to minimize the penetration depth, the ns-laser experiments were performed with a wavelength of 355 nm. For the detection of Ca^{2+} in the peripheral cell wall a fluence of the ns laser of $360\,J/cm^2$ was necessary in order to achieve a signal to noise ratio of 10. Even for a ns-laser fluence much below this value the cell wall was destroyed completely with one laser shot. Moreover, as displayed in Fig. 6a and b, the shape of the ablation area changed from shot to shot. The ablation area resembled the subjacent cell structure and cannot be attributed to the laser-beam profile. In the case of fs-laser ablation a laser fluence regime can be found where the peripheral cell wall was not destroyed. More importantly, the plasma luminescence was intense enough that Ca^+ lines could be detected with our equipment. Figure 6b displays a representative interference microscopy image of the ablation zone of the peripheral cell wall. Five fs-laser shots were needed in order to identify the ablation zone in the complex morphology of the peripheral cell wall. The ablation area is contained in a circle with a diameter of $3.5 \pm 0.2\,\mu m$. The employed fs-laser fluence of $55\,J/cm^2$ is five times ($c = 0.2$) above the measured ablation threshold of $11 \pm 1\,J/cm^2$.

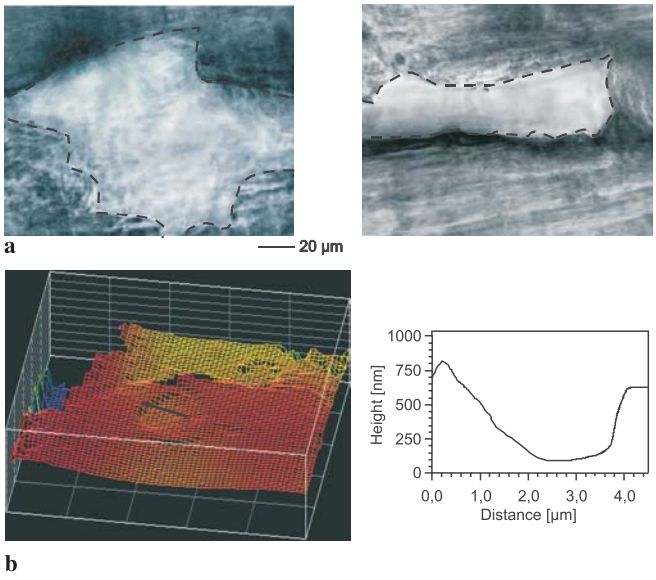

FIGURE 6 Light micrographs (**a**) from the ablated zone of the peripheral wall of a sunflower stem show the structure after a single ns-laser shot ($175\,J/cm^2$) ablation. White-light interference microscope picture of the peripheral cell wall (**b**, *left*). Five fs-laser pulses ($55\,J/cm^2$) were used to ablate the cell wall. The cross section of the ablated zone (**b**, *right*) is indicated by the *black line*

Taking into account the calculated PSF, shown in Fig. 4a (dotted line), one would not expect such a large ablation diameter for $c = 0.2$. The measured fs-laser-beam profile in the focal plane shows a Gaussian intensity distribution with a beam diameter of $4.0 \pm 0.2\,\mu m$ (see Sect. 3). For this beam diameter a c value of 0.2 leads to an ablation diameter of $3.3 \pm 0.2\,\mu m$.

The close agreement between the measured and the evaluated diameters of the ablation area demonstrates the well-defined threshold for fs-laser ablation and plasma formation. Besides the ablation area the ablation depth was also investigated. The ablation depth upon five fs-laser shots is measured for five different holes. The corresponding averaged single laser shot ablation depth is $140 \pm 25\,nm$.

In terms of analytical performance in combination with high spatial resolution for LIBS applications, this series of experiments demonstrates that fs lasers are more suitable than ns lasers.

5 Calcium analysis inside the peripheral cell wall of sunflower stems with fs-LIBS

Using fs-LIBS the bound Ca^{2+} distribution within the peripheral cell wall of sunflower hypocotyls was measured. A complete sunflower seedling (Fig. 2a) was fixed on the piezo-driven computer-controlled *xyz* stage of the microscope-type setup. Care was taken to ensure nearly con-

stant growth conditions. During the measurement, the plants are watered, in order to prevent dehydration of the cells. Therefore, the turgor pressure and the plant surface morphology were maintained. Using the light microscope, the plant surface was positioned in the focal plane of the objective. Fs-laser pulses with a fluence of $120\,\mathrm{J/cm^2}$ and $55\,\mathrm{J/cm^2}$ are used, which are 11 times ($c = 0.09$) and five times ($c = 0.2$) above the ablation threshold.

Figure 7a shows the Ca^+-line signal and the inset displays the continuum emission signal for each fs-laser shot for a laser fluence of $120\,\mathrm{J/cm^2}$. The plasma luminescence was recorded 10 ns after plasma formation within a time window of 50 ns. Each Ca^+-signal point corresponds to the integrated Ca^+-line distribution within 391–398 nm. The continuum emission signal was measured in the range between 368 nm and 375 nm. For the whole series of 200 laser shots the continuum signal stayed constant with a standard deviation of 10%. This indicates that the plasma-formation conditions do not change significantly. The Ca^+ signal drastically decreased after the first four laser shots and showed a plateau for the remaining 200 laser shots. Additional light-microscope observations showed that an outflow of cell sap was observed after three or four laser shots. Therefore, the first three Ca^+ peaks are attributed to Ca^{2+} concentrations in the peripheral cell wall, whereas the following plateau is caused by Ca^{2+} solved in vacuolar water (cell sap, see Fig. 3b). The Ca^{2+} concentrations in the peripheral cell wall are considerably higher than in the underlying tissue. In our experiments the averaged Ca^+ signal from the peripheral cell wall was three times higher than the corresponding Ca^+ signal from the vacuole of the cell.

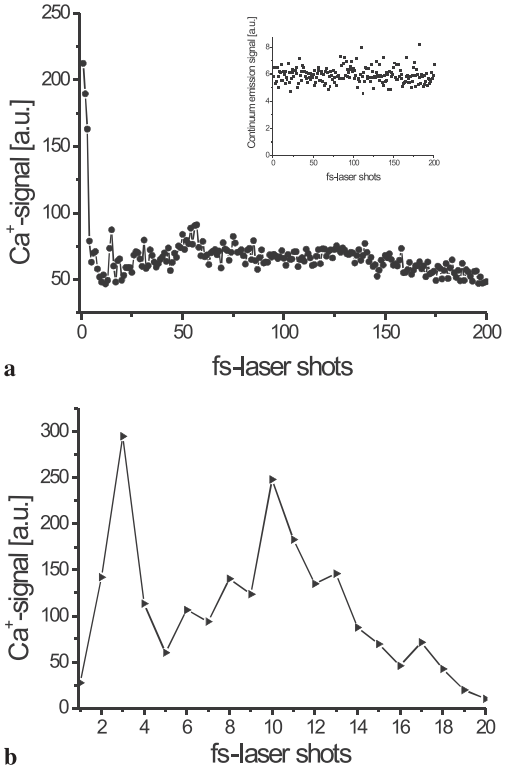

FIGURE 7 Distribution of bound calcium ions (Ca^{2+}) within the peripheral cell wall of a sunflower stem. The plasma luminescence was measured and analyzed in the spectral range from 380 nm up to 410 nm for each fs-laser shot. Integration over the Ca^+ lines at 395 nm yields the Ca^+ signal. The background signal corresponds to the integrated continuum emission in the range of 368–375 nm. **a** shows the Ca^{2+} distribution and the *inset* indicates the continuum emission signal. A laser fluence of $120\,\mathrm{J/cm^2}$ was used. **b** shows the Ca^{2+} distribution with higher resolution measured with a laser fluence of $55\,\mathrm{J/cm^2}$. a.u. = arbitrary units

At the same laser fluence of $120\,\mathrm{J/cm^2}$ the ablation depth was measured with the interference microscope. The ablation depth of around 500 nm for a single fs-laser shot can be used to estimate a wall thickness of 1.5 μm up to 2 μm. This average thickness of the peripheral cell wall is in accordance with the value measured using transmission electron micrographs [26] (Fig. 3b).

At a fs-laser fluence of $55\,\mathrm{J/cm^2}$, the Ca^+ signal from the vacuole is close to the detection limit. Nevertheless, the Ca^{2+} concentration in the peripheral cell wall can still be detected. Even for this laser fluence the axial threshold zone shows no dependence on the lateral coordinate within the peripheral cell wall and the analysis mode can be applied. The single fs-laser shot ablation depth is 140 nm.

A representative Ca^+-signal distribution is displayed in Fig. 7b. The Ca^{2+} distribution within the peripheral cell wall is shown, measured 16 mm above the root. The Ca^{2+} distribution does not decrease until 15 laser shots. The double-peak structure shows a minimum around 700 nm followed by a second maximum at around 1.4 μm. Similar double-peak structures were found at several positions along the plant stem.

6 Summary and conclusion

We investigated the analytical performance of fs-LIBS in comparison to ns-LIBS for spectrochemical *in situ* investigations of biological samples. The analytical performance was studied using Ca^{2+} detection in a water sample. For both ns- and fs-LIBS linear calibration curves were measured. The Ca^{2+} detection limit was comparable to that obtained with the ns laser. In the case of the fs-laser excitation, the continuum emission of the plasma was significantly reduced, accompanied by a faster thermalization. Moreover, the plasma-generation threshold was an order of magnitude less for the plasma produced by the fs laser.

The ablation of the peripheral cell wall of a sunflower stem was investigated both for ns-laser pulses and fs-laser pulses. For the ns laser the ablation volume varied significantly for each laser shot. The ablation zone can be attributed to the subjacent cell structure. For the laser fluence required to generate a plasma the peripheral cell wall was completely destroyed. In case of the fs laser, precise ablation conditions are found with a circular ablation zone and ablation depths below the thickness of the peripheral cell wall. More importantly, the corresponding plasma permits spectrochemical analysis out of an ablation volume in the range of femtoliters.

The analytical performance in combination with the precise laser ablation condition demonstrate that fs-laser systems are excellent light sources for highly spatial resolved LIBS on biological samples. This was demonstrated by *in situ* depth profiling of trace elements in biological samples. Bound Ca^{2+} distributions within the peripheral cell wall of a sunflower stem were resolved with an axial resolution of around 140 nm. Future research will extend this method to a minimal inva-

sive microscopy technique. Using an ICCD camera with high repetition rates, three-dimensional element-specific imaging with high spatial resolution will be demonstrated. Objectives with a higher NA provide an axial resolution below 100 nm. Due to the generality of LIBS and fs-laser ablation the technique has a broad range of possible applications in biological, medical and technical disciplines.

ACKNOWLEDGEMENTS The authors would like to thank Dr. K. Hannemann from the German Aerospace Center, DLR for the loan of the ICCD camera and the spectrometer. We gratefully acknowledge financial support by the Deutsche Forschungsgemeinschaft and the Fonds der Chemischen Industrie. We thank M. Maniak for the long-term loan of the confocal microscope and H. Hillmer for providing the interference microscope.

REFERENCES

1 D.A. Rusak, B.C. Castle, B.W. Smith, J.D. Winefordner: Trends Anal. Chem. **17**, 453 (1998)
2 D. Kossakovski, J.L. Beauchamp: Anal. Chem. **72**, 4731 (2000)
3 L. St-Onge, M. Sabsabi: Spectrochim. Acta Part B: At. Spectrosc. **55**, 299 (2000)
4 D. Romero, J.J. Laserna: Spectrochim. Acta Part B **55**, 1241 (2000)
5 J.M. Vadillo, C.C. Garcia, S. Palanco, J.J. Laserna: J. Anal. At. Spectrom. **13**, 793 (1998)
6 A. Kaiser, B. Rethdeld, M. Vicanek, G. Simon: Phys. Rev. B **61**, 11 437 (2000)
7 B.C. Stuart, M.D. Feit, A.M. Rubenchik, B.W. Shore, M.D. Perry: Phys. Rev. Lett. **74**, 2248 (1995)
8 B.C. Stuart, M.D. Feit, S. Herman, A.M. Rubenchik, B.W. Shore, M.D. Perry: Phys. Rev. B **53**, 1749 (1996)
9 J. Krüger, W. Kautek, M. Lenzner, S. Sartania, C. Spielmann, F. Krausz: Appl. Surf. Sci. **127–129**, 892 (1998)
10 R. Stoin, D. Ashkenasi, A. Rosenfeld, E. Campbell: Phys. Rev. B **62**, 13 167 (2000)
11 A.C. Tien, S. Backus, H.C. Kapteyn, M.M. Murnane, G. Mourou: Phys. Rev. Lett. **82**, 3883 (1999)
12 J. Bonse, M. Geuß, S. Baudach, H. Sturm, W. Kautek: Appl. Phys. A **69**, 399 (1999)
13 X. Zhu, D.M. Villeneuve, A.Y. Naumov, S. Nikumb, P.B. Corkum: Appl. Surf. Sci. **152**, 138 (1999)
14 O. Lehmann, M. Stuke: Appl. Phys. Lett. **67**, 338 (1995)
15 C. Momma, B.N. Chichkov, S. Nolte, F. von Alvensleben, A. Tünnermann, H. Welling, B. Welleghausen: Opt. Commun. **129**, 134 (1996)
16 D. von der Linde, K. Sokolowski-Tinten, J. Bialkowski: Appl. Surf. Sci. **109–110**, 1 (1997)
17 B.N. Chichkov, C. Momma, F. von Alvensleben, A. Tünnermann: Appl. Phys. A **63**, 109 (1996)
18 M.D. Feit, A.M. Rubenchik, B.-M. Kim, L.B. da Silva, M.D. Perry: Appl. Surf. Sci. **127–129**, 869 (1998)
19 B.-M. Kim, M.D. Feit, A.M. Rubenchik, B.M. Mammini, L.B. da Silva: Appl. Surf. Sci. **127–129**, 857 (1998)
20 F.H. Loesel, M.H. Niemz, J.F. Bille, T. Juhasz: J. Quantum Electron. **32**, 1717 (1996)
21 A.A. Oraevsky, L.B. da Silva, A.M. Rubenchik, M.D. Feit, M.E. Glinsky, M.D. Perry, B.M. Mammini, W. Small, B.C. Stuart: IEEE J. Sel. Top. Quantum Electron. **2**, 801 (1996)
22 V. Margetic, A. Pakulev, A. Stockhaus, M. Bolshov, K. Niemax, R. Hergenröder: Spectrochim. Acta Part B **55**, 1771 (2000)
23 B. Le Drogoff, J. Margot, M. Chaker, M. Sabsabi, O. Barthélemy, T.W. Johnston, S. Laville, F. Vidal, Y. von Kaenel: Spectrochim. Acta Part B **56**, 987 (2001)
24 K.L. Eland, D.N. Stratis, D.M. Gold, S.R. Goode, S.M. Angel: Appl. Spectrosc. **55**, 286 (2001)
25 R. Netz, T. Feurer, R. Wolleschensky, R.A. Sauerbrey: Appl. Phys. B **70**, 833 (2000)
26 U. Kutschera: Planta **181**, 316 (1990)
27 J. Deitche, M. Kempe, W. Rudolph: J. Microsc. **174**, 69 (1994)
28 E.J.B. Pawley: *Handbook of Biological Confocal Microscopy* (Plenum, New York 1995)
29 T.R. Corle, G.S. Kino: *Confocal Scanning Optical Microscopy and Related Imaging Systems* (Academic, San Diego, CA 1996)
30 B. Le Drogoff, J. Margot, M. Chaker, M. Sabsabi, O. Barthélemy, T.W. Johnston, S. Laville, F. Vidal, Y. von Kaenel: Spectrochim. Acta Part B **56**, 987 (2001)
31 C.H. Fan, J. Sun, J.P. Longtin: J. Appl. Phys. **91**, 2530 (2002)
32 J. Noack, A. Vogel: IEEE J. Quantum Electron. **35**, 1156 (1999)
33 A. Vogel, J. Noack, K. Nahen, D. Theisen, S. Busch, U. Parlitz, D.X. Hammer, G.D. Noojin, B.A. Rockwell, R. Birngruber: Appl. Phys. B **68**, 271 (1999)
34 U. Kutschera: Rev. Bras. Fisiol. Veg. **65**, 66 (2000)